이중목 노즐 개념에 기반한 유체 추력벡터제어에 관한 연구

Kexin Wu[a] · 김희동[a,*]

Study on Fluidic Thrust Vector Control Based on Dual-Throat Concept

Kexin Wu[a] · Heuy Dong Kim[a,*]

[a]*Department of Mechanical Engineering, Andong National University, Korea*
Corresponding author. E-mail: kimhd@anu.ac.kr

ABSTRACT

Numerical simulations were carried out in a supersonic nozzle to investigate the possibility of using dual-throat nozzle concept in fluidic thrust vector control. Validation of the methodology showed an excellent agreement between the computational fluid dynamics results and the experimental data available, which were based on the well-assessed SST k-ω turbulence mode. The deflection angle, system resultant thrust ratio, and thrust efficiency were investigated in a wide range of nozzle pressure ratios and injection pressure ratios. The performance variations of the dual-throat nozzle thrust vector control system were clearly illustrated with this two-dimensional computational domain. Some constructive conclusions were obtained that may be used as a reference for further studies in the fluidic thrust vector control field.

초   록

유체 추력벡터 제어에서 이중목 노즐 개념의 이용 가능성을 조사하기 위하여, 초음속 노즐에서 수치해석을 수행하였다. 수치해석 검증에서 SST k-ω 난류모델을 사용하여 실험결과를 잘 구현하였다. 광범위한 노즐 압력비와 분사 압력비에서 편향각도, 시스템의 전체 추력비 및 추력 효율을 조사하였다. 본 연구에서 이중목 노즐의 추력벡터제어 시스템의 성능 변화는 2차원 계산영역에서 명확하게 설명되었다. 본 연구에서 얻어진 결과들은 유체추력벡터제어 분야에 중요한 기초자료를 제공할 것이다.

Nomenclature

C_{sys} : system resultant thrust ratio

F_{ideal} : ideal isentropic thrust

$F_{I,i}$: ideal isentropic thrust of injected flow

$F_{I,p}$: ideal isentropic thrust of primary flow

F_x : axial force

F_y : normal force

H : throat height

H_{t1} : upstream throat height of the nozzle

H_{t2} : downstream throat height of the nozzle

IPR : injection pressure ratio, $IPR=P_i/P_b$

L : length of dual-throat nozzle cavity

m_p : mass flow rate of the primary flow

m_i : mass flow rate of the injection flow

NPR: nozzle pressure ratio, $NPR=P_0/P_b$

P_0 : stagnation pressure

P_b : ambient pressure

P_e : area-weighted average static pressure of the dual-throat nozzle exit

P_w : static pressure along the upper wall

R : gas constant

T : temperature

T_0 : stagnation temperature

X : distance along the horizontal direction

γ : ratio of specific heats

η : thrust efficiency

δ_β : deflection angle

θ_1 : upstream divergent cavity angle

θ_2 : downstream convergent cavity angle

1. Introduction

In recent decades, the fluidic thrust vector control (FTVC) is growing a more and more important technique to redirect the thrusts of the air vehicles. A lot of benefits are obtained, such as the replacement of complex mechanical parts, better maneuverability and perfect control effect[1-3]. The aircraft with the FTVC technique can take off and land at a very short distance on an aircraft carrier. Herbst[4] guessed that the FTVC will be the most promising development direction in the future. Moreover, Chambers[5] illustrated that this FTVC technique can be used to maintain the excellent control effectiveness under stalled operating conditions. A series of methods are utilized in FTVC field to control the deflection degree of primary jet, such as shock vector control (SVC), co-flow or counter-flow thrust vector control (Co- or Counter-FTVC), throat-shifting thrust vector control (TSTVC), and dual-throat nozzle thrust vector control (DTNTVC). Deng et al.[6-7] utilized the shock wave to carry out the studies of the FTVC and reported the effects of some factors as follows: NPR, injection location, and bypass flow ratio. However, the induced shock waves always reduce the system resultant thrust ratio. Deere[8] demonstrated that throat-shifting technique could offer a larger system resultant thrust ratio, but the deflection degree is very less compared with SVC method. Wu et al.[9] investigated the counter-flow TVC method and illustrated that it can generate very large deflection angle with less secondary mass flow ratio, but it is difficult to address the problems of suction supply sources.

In this paper, the DTNTVC technique is investigated emphatically due to the higher thrust vector efficiency without sacrificing other performance than other fluidic thrust techniques. Actually, the dual-throat technique was developed from the throat-shifting method for improving the boundedness[10]. An experiment was carried out at the NASA Langley Research Center and some reliable experiment data were obtained by Flamm et al.[11]. The sketch of the DTNTVC system is shown in Fig. 1. It can be seen that the recessed cavity is situated between the upstream throat (Throat 1) and downstream throat (Throat 2), and an injector is located at
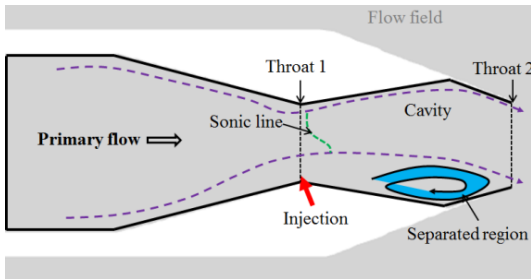
Fig. 1 Sketch of the dual-throat.

the upstream throat. The primary flow is skewed by the injected flow and separated region is formed below the cavity.

2. Computational domain

The experimental and computational models with detailed geometry dimensions are depicted in Fig. 2. The experimental setups were established at the NASA Langley Research Center and the tests were conducted at static conditions in the Jet Exit Test Facility [11]. As shown in Fig. 2(a), the dual-throat nozzle is installed within the test devices to conduct the experiment. The identical nozzle with detailed dimensions utilized in the numerical simulations is shown in Fig. 2(b). The second convergent part of the dual-throat nozzle is designed according to the same throat dimension of traditional C-D nozzle and the cavity is formed between two throats. The physical dimensions of upstream and downstream throat heights are $H_{t1}=H_{t2}=29.21$ mm. The length of the cavity $L=76.20$ mm. The divergent and convergent ramp angles of the cavity are $10°$ and $20°$ respectively. A secondary flow is injected at the upstream throat, which is from an injection slot with the width of 0.55 mm. The injection angle is set as $150°$ in all simulations.
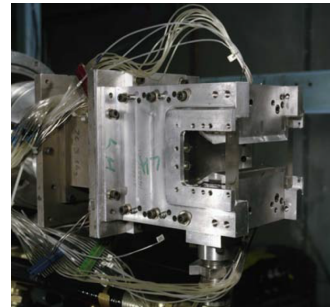
a) Experimental model
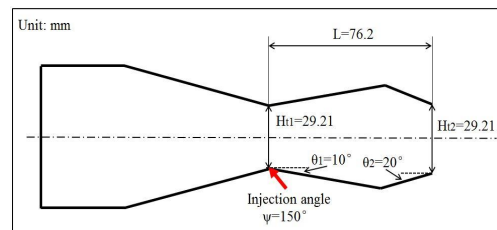
b) Computational model

Fig. 2 Experimental and computational models of the dual-throat nozzle.

The commercial software ANSYS Fluent 17.1 was used as the solver and Gambit was utilized to create the 2D computational domain and mesh. The working gas was air assumed as an ideal gas. Viscous flows were calculated by resolving Navier-Stokes equations. Second order accuracy was selected to reveal the details of the flow-field as much as possible. The boundary conditions in present numerical simulations are clearly shown in Fig. 3. Pressure inlet was used to define the boundaries of the primary flow inlet (P_0) and injected flow inlet (P_i). The exit boundaries of the computational domain were set as the pressure outlet ($P_b=1$ atm). The stagnation temperature was kept at 300 K. The mass flow rates of the pressure inlet and outlet were monitored. As the difference of the mass flow rate is less than 10^{-5}, the case can be judged as the convergent solution.
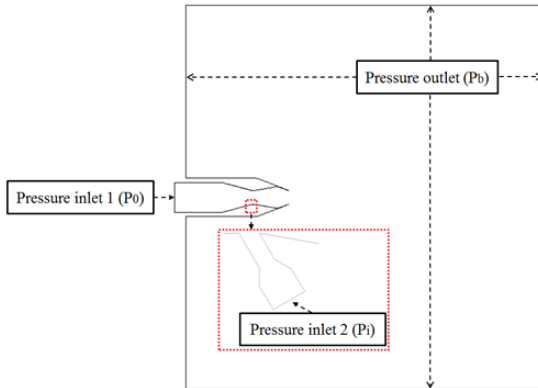
Fig. 3 Computational domain and boundary conditions.

Fig. 4 Comparison of upper wall pressure distributions between the CFD result and the experimental data.

3. Results and discussions

3.1 Validation

The methodology is validated with the experimental data of Flamm et al.[11] reported in the literature. In compressible gas dynamics field, the SST k-ω turbulence model is recognized as the most suitable to conduct the simulations for various supersonic flows. Deng et al.[6] conducted the simulations of SVC with SST k-ω turbulence model and validated well with the experimental result. Shi et al.[12] carried out the validation with all kinds of turbulence models and illustrated that the SST k-ω turbulence model gives the best agreement with the experimental data. Thus, the SST k-ω turbulence model is selected to validate the experimental data in this paper. As depicted in the Fig. 4, normalized pressure distribution along the upper wall of the dual-throat nozzle is compared with the experimental data at NPR=4, IPR=7.6. It can be observed that the SST k-ω turbulence model shows an accurate prediction in agreement with the experimental data available. Therefore, the SST k-ω turbulence model is used for further simulations.
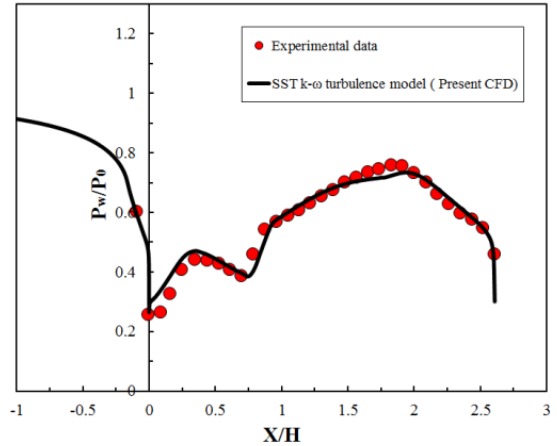
In order to provide insight into the internal flow characteristics, Fig. 5 depicts the comparison between the experimental shadowgraph image and density contour from the CFD result at NPR=4, IPR=7.6. The experimental shadowgraph image illustrates that the mainstream attaches to the upper wall of the cavity and shock waves are formed in the vicinity of the upstream nozzle throat. The sonic line is skewed and separation region is formed at the bottom of the cavity, which result in the deflection of mainstream. In addition, some shock waves are existed at the exit of dual-throat nozzle. Compared with the density contour of the present CFD result, it is evident that the present simulations can predict the performance variation accurately.

3.2 DTNTVC performance at various NPRs

In this section, the performances of the DTNTVC system are studied at various NPRs by keeping the IPR constant at 7.6.

In Fig. 6, it depicts the variation of performance parameter in terms of deflection angle by changing the NPR value. At IPR=7.6,

different NPR values from 2 to 6.5 are varied. The calculated deflection angle is defined as follow:

$$\delta_\beta = \tan^{-1}(\frac{F_y}{F_x}) \qquad (1)$$

Firstly, present CFD result is compared with the exclusive thrust vector angle acquired from the experimental data [11]. The deflection angle calculated by Eq. 1 is fitting perfectly with the experimental data available. In addition, the deflection angle is found to be decreasing with the increase of NPR value and it reaches the maximum value at NPR=2. The power of primary flow becomes stronger with the increase of NPR value. Moreover, the deflection degree of the skewing sonic line becomes weaker with the increase of NPR value. Hence, the deflection degree is smaller with the increase of NPR at the fixed IPR value.

In Fig. 7, it can be clearly seen that system resultant thrust ratio increases with the increase of NPR at IPR=7.6. The system resultant thrust ratio is given as follow:

$$C_{sys} = \frac{\sqrt{Fx^2+Fy^2}}{F_{ideal}} = \frac{\sqrt{Fx^2+Fy^2}}{F_{I,p}+F_{I,i}}$$
$$= \frac{\sqrt{Fx^2+Fy^2}}{m_p\sqrt{\frac{2\gamma RT_0}{\gamma-1}[1-(\frac{1}{NPR})^{\frac{\gamma-1}{\gamma}}]}+m_i\sqrt{\frac{2\gamma RT_0}{\gamma-1}[1-(\frac{1}{NPR \cdot IPR})^{\frac{\gamma-1}{\gamma}}]}} \qquad (2)$$

Even though the ideal isentropic thrust (F_ideal) increases with the increase of NPR value, the more rapid increase of real resultant thrust results in a larger system resultant thrust ratio at higher NPR value based on the Eq. 2. The lowest level is obtained at NPR=2, but the proportion of real resultant thrust is more than 85% of the ideal thrust. The excellent thrust vector performance is proved

based on the dual-throat nozzle vector control technology.

A comparison on the thrust efficiency at various NPRs is presented in Fig. 8. The definition of the thrust efficiency is given as:

$$\eta = \frac{\delta_\beta}{(\frac{m_i}{m_i+m_p}) \cdot 100} \qquad (3)$$

It means that the effective thrust vector angle caused by per unit injected flow increases with the increase of the NPR value. In addition, the highest thrust efficiency is gained at NPR=6.5 when the IPR value is fixed at 7.6.

3.3 DTNTVC performance at various IPRs

In this section, the performance of the DTNTVC is studied at various IPRs by keeping the NPR value constant at 4.

The performance of the DTNTVC in terms of thrust vector angle is reported in Fig. 9. The positive value represents the positive deflection (Y+ direction) and the negative value means the opposite deflection (Y-direction). For the validation of deflection angle, the present CFD result gives an excellent agreement with the experimental data available. For all the operating conditions, deflection angles are positive except for IPR=2. At IPR=0, there is no injected mass flow rate from the injector, which cannot result in any deflection degree. The deflection angle increases rapidly with the increase of IPR value, while 2<IPR<7. Then it follows by a smooth enhancement. Combined with the Mach number contours and streamlines as shown in Fig. 12, these variations can be explained very well. It can be observed that the separation region is located at the top of
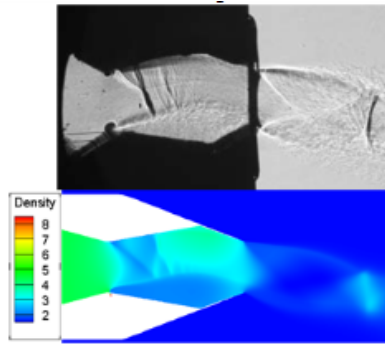
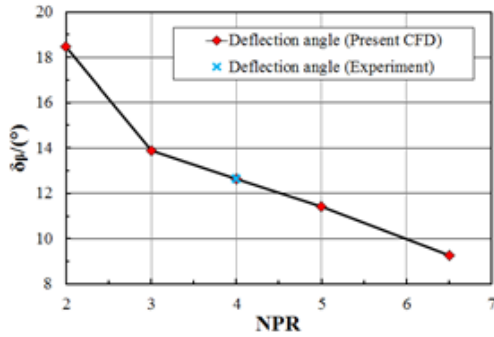Fig. 5 Experimental shadowgraph and computational density contour at NPR=4, IPR=7.6.

Fig. 6 Deflection   angles   at   various   NPRs (IPR=7.6).

Fig. 7 System resultant thrust ratios at various NPRs (IPR=7.6).

Fig. 8 System resultant thrust ratios at various NPRs (IPR=7.6).

the cavity for IPR=2. It results in the opposite deflection direction, compared with other working conditions. Moreover, the area of separation region increases with the increase of the IPR value. However, the separation region area increases slowly when the IPR value is reached 7. This is corresponding to the smooth and slow increase of the deflection angle.

A comparison on the system resultant thrust ratio at various IPRs is shown in Fig. 10. It illustrates that the system resultant thrust ratio decreases with the increase of IPR value. Based on the Eq. 2, the ideal isentropic primary flow thrust ($F_{I,p}$) is constant and ideal isentropic injection flow thrust ($F_{I,i}$) increases with the increase of IPR value. Meanwhile, the
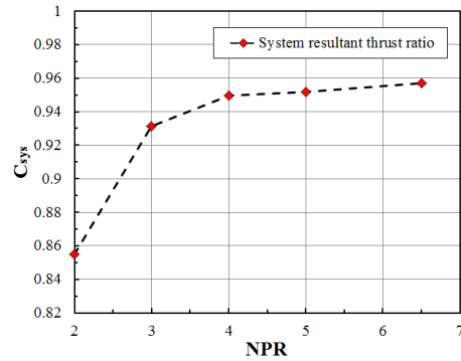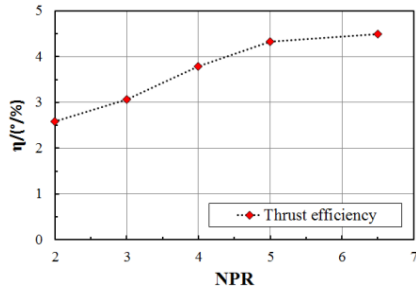
real resultant thrust decreases with the increase of the IPR value. Thus, it results in the decrease of the system resultant thrust ratio. The high system resultant thrust ratio of the DTNTVC is proved by the data that the lowest system resultant thrust ratio is more than 0.93 at IPR=10.

A series of computational thrust efficiencies are obtained in order to distinguish the effect of the IPR on redirecting the thrust in Fig. 11. The highest level of thrust efficiency is presented at IPR=3. Based on the Eq. 3, it can be obtained that the deflection angle caused by per unit injected flow is highest at IPR=3. At 0<IPR<3, the thrust efficiency increases with the increase of IPR value. Even though the deflection angle is small, the injected flow ratio   is   more   suitable   to   result   in
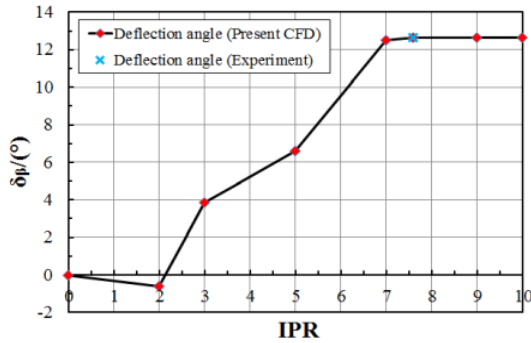
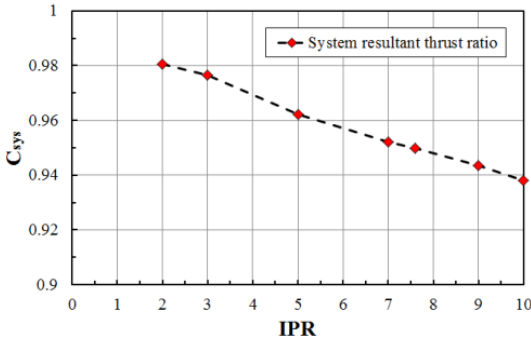Fig. 9 Deflection angles at various IPRs (NPR=4).
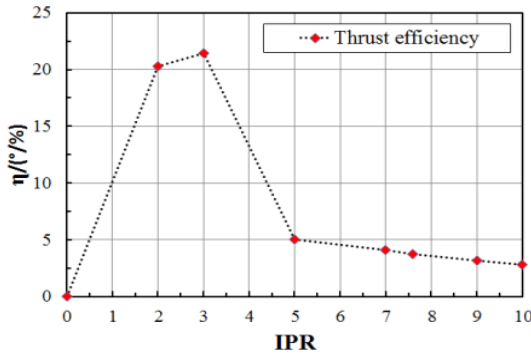

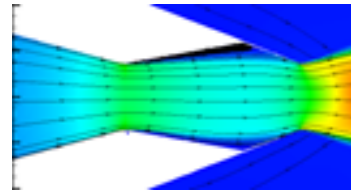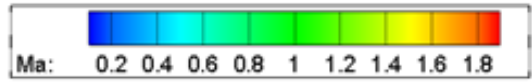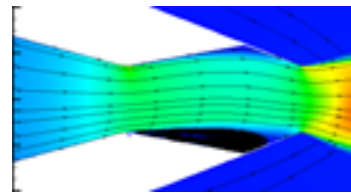Fig. 10 System resultant thrust ratio at various IPRs (NPR=4).

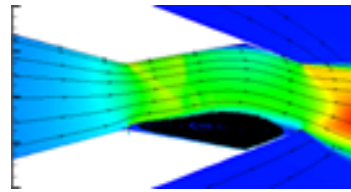Fig. 11 Thrust efficiency at various IPRs (NPR=4).

the larger thrust efficiency. Especially, the thrust efficiency is zero at IPR=0, because there is no deflection angle at this moment. As the IPR value exceeds 3, the thrust efficiency decreases with the increase of IPR value.
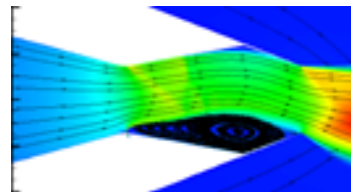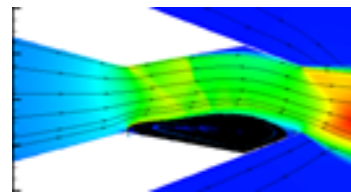

a) IPR=2

b) IPR=3

c) IPR=7

d) IPR=7.6

e) IPR=9

Fig. 12 Mach number contours and streamlines at various IPRs (NPR=4).

4. Conclusions

The FTVC using dual-throat concept was studied and the effects of NPR and IPR were illustrated respectively. Meanwhile, the core performance parameters were reported in this paper, such as deflection angle, system resultant thrust ratio, and thrust efficiency. Present CFD results were compared with the experimental data to validate the reliability of the methodology. It was evident that there is an excellent agreement between the present CFD and experimental results. The important conclusions of the present study are illustrated as follows:

At IPR=7.6, the deflection angle is found to be increased with the decreasing of NPR value. The system resultant thrust ratio increases with the increase of the NPR as well as thrust efficiency. The high efficiency of the DTNTVC system is testified.

By fixing NPR=4, the deflection angle increases rapidly with the increase of the IPR value at 3<IPR<7. As IPR is more than 7, the thrust vector angle follows by a smooth and slow increase with the continuous increase of the IPR value. The system resultant thrust ratio decreases continually as the IPR value increases. The highest thrust efficiency is obtained at IPR=3. As the IPR value is more than 3, the thrust efficiency decreases with the increase of IPR value.

Acknowledgment

References

1. Mason, M.S. and Crowther, W.J., "Fluidic Thrust Vectoring for Low Observable Air Vehicles," *2nd AIAA Flow Control Conference*, O.R., USA, AIAA 2007-5084, 2004.

2. Asbury, S.C. and Capone, F.J., "High-alpha Vectoring Characteristics of the F-18/HARV," *Journal of Propulsion and Power*, Vol. 10, No. 1, pp. 116-121, 1994.

3. Henderson, W.P., "Propulsion System Integration in High Performance Aircraft," *Journal of Aerospace Engineering*, Vol. 10, pp. 21-25, 1990.

4. Herbst, W.B., "Future Fighter Technologies," *Journal of Aircraft*, Vol. 17, No. 8, pp. 561-566, 1980.

5. Chambers, J.R., "High-alpha Flight Dynamics: Lessons Learned," *4th Applied Aerodynamics Conference, Fluid Dynamics and Co-Located Conference*, S.D., AIAA 86-1774-CP, 1986.

6. Deng, R.Y., Kong, F.S. and Kim, H.D., "Numerical Simulation of Fluidic Thrust Vectoring in an Axisymmetric Supersonic Nozzle," *Journal of Mechanical Science and Technology*, Vol. 28, No. 12, pp. 4979-4987, 2014.

7. Deng, R.Y. and Kim, H.D., "A Study on the Thrust Vector Control Using a Bypass Flow Passage," *Proceeding of the Institution of Mechanical Engineers, Part G: Journal of Aerospace Engineering,* Vol. 229, No. 9, pp. 1722-1729, 2015.

8. Deere, K.A., "Summary of Fluidic Thrust Vectoring Research Conducted at NASA Langley Research Center," *21th AIAA Applied Aerodynamics Conference*, O.R., AIAA 2003-3800, 2003.

9. Wu, K.X., Kim, H.D. and Jin, Y.Z., "Fluidic Thrust Vector Control Based on Counter-Flow Concept," *Proceeding of the Institution of Mechanical Engineers, Part G: Journal of Aerospace Engineering,* pp. 1-11, 2018.

10. Deere, K.A., Berrier, B.L., Flamm, J.D. and Johnson, S.K., "Computational Study of Fluidic Thrust Vectoring Using Separation Control in a Nozzle," *21st AIAA Applied Aerodynamics Conference, Fluid Dynamics and Co-Located Conference,* O.R., USA, AIAA 2003-3803, 2003.

11. Flamm, J.D., Deere, K.A., Berrier, B.L. and Johnson, S.K., "Design Enhancements of the Two-Dimensional, Dual Throat Fluidic Thrust Vectoring Nozzle Concept," *3rd AIAA Flow Control Conference*, S.F., USA, AIAA 2006-3701, 2006.

12. Shi, J.W., Zhou, L., Wang, Z.X. and Sun, X.L., "Investigation on Flowfield Characteristics and Performance of Shock Vector Control Nozzle Based on Confined Transverse Injection," *Journal of Engineering for Gas Turbines and Power*, Vol. 138, No. 101502, pp. 1-11, 2016.